

# Correlation between relativistic reflection fraction and photon index in *NuSTAR* sample of Seyfert 1 AGN

Savithri H. Ezhikode,<sup>1,3\*</sup> Gulab C. Dewangan,<sup>1†</sup> Ranjeev Misra,<sup>1‡</sup>  
Ninan Sajeeth Philip<sup>1,2,3</sup>

<sup>1</sup> Inter-University Centre for Astronomy & Astrophysics, Post Bag 4, Ganeshkhind, Pune, India

<sup>2</sup> Artificial Intelligence Research and Intelligent Systems. Thelliyoor, Kerala - 689644, India

<sup>3</sup> Department of Physics, St. Thomas College, Kozhencerry, Kerala 689641, India

Accepted 2020 April 22. Received 2020 April 6; in original form 2019 November 27

## ABSTRACT

The primary X-ray emission from AGN, described by a power law, irradiates the accretion disc producing reflection features in the spectrum. The reflection features arising from the inner regions of the disc can be significantly modified by the relativistic effects near the black hole. We investigate the relationship between the relativistic reflection fraction  $R_f$ , defined as the ratio of the coronal intensity that illuminates the accretion disc to the coronal intensity observed directly, and the hard X-ray photon index  $\Gamma$  of a *NuSTAR* sample of Seyfert 1 galaxies. The X-ray spectra are modelled using RELXILL code which helps to directly obtain the reflection fraction of a relativistically smeared reflection component. The parameter  $R_f$  depends on the amount of Comptonised X-ray emission intercepted by the inner accretion disc. We found a positive correlation between  $\Gamma$  and  $R_f$  in our sample. Seed photons from a larger area of an accretion disc entering the corona will result in increased cooling of the coronal plasma, giving rise to steeper X-ray spectrum. The corona irradiating the larger area of the disc will result in higher reflection fraction. Thus, the observed  $R_f - \Gamma$  relation is most likely related to the variations in the disc-corona geometry of AGN.

**Key words:** galaxies:active – galaxies:Seyfert – X-rays:galaxies

## 1 INTRODUCTION

The X-ray spectra of Seyfert 1 galaxies are composed of several components, apart from the underlying power law continuum. A portion of the primary X-ray power law photons, believed to be produced by the Comptonisation of the optical/UV photons from the accretion disc by the hot electrons in the corona (Haardt & Maraschi (1993)), irradiate the accretion disc and the circumnuclear material. This primary continuum gets reprocessed producing the reflection features in the X-ray band (e.g. George & Fabian (1991); Matt et al. (1991); Reynolds (1999); Fabian & Ross (2010)), making a complex broadband spectrum.

The hard X-ray spectrum of AGN consists of a hump-like feature around 20–40 keV. This reflection hump is produced as a result of the interaction of the primary X-ray photons with the cold gas. The hard X-ray photons irradiating the optically-thick material are Compton

backscattered whereas the softer X-rays are photoelectrically absorbed (Nandra et al. 1990; Nandra & Pounds 1994; Lightman & White 1988; Fabian & Ross 2010), leading to the reflection hump. At energies below 20 keV, there is a deficit in the spectrum due to the absorption mainly by iron. In addition, the incident X-rays can be reprocessed into fluorescent emission lines. The Fe K $\alpha$  line emission at 6.4 keV is the strongest among these. Since the reflection features are dependent on the structure, temperature, chemical composition and ionisation state of the gas, the reflection spectrum in AGN can give direct information about the physical conditions in the reflecting medium.

The observed Fe K $\alpha$  emission line generally consists of a narrow and a broad component. The narrow line is attributed to the emission by fluorescence from distant (and low velocity) materials like the cold torus or the outer BLR. On the other hand, the broad Fe K $\alpha$  emission line is thought to be arising from the inner part of the accretion disc. The effects of Doppler boosting, light-bending and gravitational redshift can change the width and profile of the emission lines originating from regions near the supermassive black hole (SMBH) (Fabian et al. 1989,

\* E-mail: savithri@iucaa.in

† E-mail: gulabd@iucaa.in

‡ E-mail: rmisra@iucaa.in

2000; Fabian & Vaughan 2003; Reynolds & Nowak 2003; Dovčiak et al. 2004; Miller et al. 2008; Steiner et al. 2011; Reynolds et al. 2012; Dauser et al. 2012). Hence the broadening of Fe K $\alpha$  emission line provides vital information on the reflection from inner regions of the accretion disc.

The observed hard X-ray spectrum of AGN is a combination of the reflection spectrum and the primary power law. Since the reflection component emerges due to the irradiation of a fraction of the primary X-rays on the accretion disc, the strength of reflection can be obtained from the ratio of the fluxes from the reflected emission and the direct emission. A parameter for the reflection fraction for relativistic case was first introduced in the relativistic reflection model RELXILL (García et al. 2014; Dauser et al. 2016). More details of this model are given in Section 3. As the amount of reflection could be modified by the area of the reflector and the location of the X-ray emitting region, the reflection fraction can provide important information regarding the geometry of the accretion disc and the corona.

A number of studies have discussed the connection between the geometry of corona and the reflection. In a study of black hole candidate GX 339-4, Ueda et al. (1994) observed a correlation between the intrinsic spectral slope and the amount of reflection which may be explained by a change in the relative geometry of the corona and accretion disc. Later, Zdziarski et al. (1999) found a strong correlation between the intrinsic X-ray spectral slope and the amount of Compton reflection in Seyferts. This indicates the role of the cold reflecting medium as a source of seed photons for thermal Comptonisation in the hot plasma. Wilkins & Gallo (2015) discussed the effect of the geometry of the corona on the relativistically blurred X-ray reflection arising from the accretion discs of AGN. They showed that low reflection fractions (ratio of the reflected flux to the continuum flux) in AGN might be observed when a patchy corona covers a large portion ( $\gtrsim 85\%$ ) of the innermost regions of the disc and Compton scatter the reflected X-rays from this region. It has also been previously reported that the amount of reflection is stronger in low-luminosity Seyferts than the high-luminosity, high-redshift sources (Reeves & Turner 2000; Page et al. 2005; Shemmer et al. 2008).

This work focuses on the relativistic reflection fraction  $R_f$  of Seyfert 1 galaxies. This can be achieved by analysing the data from *Nuclear Spectroscopic Telescope Array* (*NuSTAR*; Harrison et al. (2013)), a hard X-ray observatory with high sensitivity in the 3–79 keV band. We have used the *NuSTAR* observations of many Seyferts for this study. The high-quality spectra from *NuSTAR* helped to get better constraints on the coronal properties and other physical parameters of AGN, in the past few years (e.g. Brenneman et al. (2014); Baloković et al. (2015); Fabian et al. (2015, 2017); Matt et al. (2015); Marinucci et al. (2014, 2015, 2016); Landt et al. (2017); Pahari et al. (2017); Tortosa et al. (2017, 2018); Rani & Stalin (2018); Frederick et al. (2018); Middei et al. (2018); Ghosh et al. (2018)). A number of works on individual AGN or sample of AGN have also focussed on the X-ray reflection features using *NuSTAR* data (e.g. Zoghbi et al. (2015); Xu et al. (2017); Buisson et al. (2018); Porquet et al. (2018)).

This paper is organised as follows. In Section 2, we present the sample selection and data reduction methods. Detailed modelling of individual AGN spectra is described

in Section 3. We discuss our results in Section 4. The summary of the work is given in Section 5.

## 2 SAMPLE SELECTION & DATA PROCESSING

We compiled the list of all AGN given in the *NuSTAR* Master Catalog NUMASTER as available on July 2019 from HEASARC archive. This initial sample consists of a total of 227 Seyfert type 1 (Sy 1) AGN observed in the SCIENCE mode. The sample includes Sy 1.0, Sy 1.2, Sy 1.5, Sy 1.8, Sy 1.9, Sy 1i, Sy 1h and some sources with unknown classification. We searched for the sub-classification of these sources using Simbad<sup>1</sup>, NED<sup>2</sup>, HyperLeda<sup>3</sup>, and literature and found that there were 66 unobscured sources (Sy 1.0, Sy 1.2, & narrow-line Seyfert 1 (NLS1)) in the sample. From this sample we selected sources with exposure time  $\geq 50$  ks and *Swift*-BAT flux  $\geq 10^{-11}$  erg cm $^{-2}$ s $^{-1}$  in order to get high-quality spectra. This resulted in a sample size of 23 sources which belong to the classes Sy 1.0, Sy 1.2 and NLS1.

The *NuSTAR* data for the 23 unobscured sources were compiled and then reduced with the standard pipeline in the *NuSTAR* Data Analysis Software (NUSTARDAS v1.6.0). For sources with multiple observations, we used the one with the longest exposure time. The data were processed for both Focal Plane Modules, FPMA and FPMB, using the calibration files taken from the *NuSTAR* CALDB (version 20160731). The cleaned and calibrated Level-2 event files were created using the `nupipeline` task. Further, the software module `nuproducts` was used to generate the source and background spectra from the filtered event lists. The spectra were extracted from circular regions of different sizes depending on the source. However, the source and background spectra of each observation were extracted from regions of the same size.

### 2.1 Final Sample

The relativistic effects in the vicinity of SMBH lead to the broadening of the Fe K $\alpha$  lines in the AGN spectrum. Therefore, objects that have broad Fe emission lines are suitable for estimating the relativistic reflection fraction. The significance of Fe emission lines in the sample was verified by fitting the spectrum using XSPEC version: 12.9.0. Cosmological parameters of  $H_0 = 70$  km s $^{-1}$  Mpc $^{-1}$ ,  $\Omega_\Lambda = 0.73$  and  $\Omega_M = 0.27$  are used throughout this paper, and the errors quoted correspond to 90% confidence level. The spectral fitting procedure we followed for identifying the broad Fe line is explained below.

The spectra were first fitted with the power law model (POWERLAW) corrected for Galactic absorption. We modelled the Galactic X-ray absorption with TBABS using the Galactic column density  $N_H^{\text{Gal}}$  taken from LAB Survey (Kalberla et al. 2005). Since the spectra from FPMA and FPMB were fitted simultaneously, the model CONSTANT was used for accounting the cross-calibration differences between

<sup>1</sup> <http://simbad.u-strasbg.fr/simbad/>; Wenger et al. (2000)

<sup>2</sup> <https://ned.ipac.caltech.edu/>

<sup>3</sup> <http://leda.univ-lyon1.fr/>; Makarov et al. (2014)

**Table 1.** Details of the sample of Seyferts with *NuSTAR* observations. The count rate is obtained for the 3–79 keV band.

No.	Object	RA	DEC	$z$	Observation	Obs. Date	Exposure	Count Rate
		degrees	degrees		ID	yyyy-mm-dd	s	$10^{-2}$ count s $^{-1}$
1	3C 382	278.76413	32.69633	0.058	60001084002	2013-12-18	82585	81.46±0.32
2	4C 74.26	310.65545	75.13401	0.104	60001080006	2014-10-30	90925	74.94±0.29
3	Ark 120	79.04759	-0.14983	0.033	60001044004	2014-03-22	65458	74.30±0.34
4	Ark 564	340.66394	29.72536	0.025	60101031002	2015-05-22	211226	28.60±0.12
5	ESO 141-G 055	290.30890	-58.67031	0.037	60201042002	2016-07-15	93011	67.16±0.27
6	Fairall 9	20.94074	-58.80578	0.047	60001130003	2014-05-09	93838	57.10±0.25
7	IC 4329A	207.33028	-30.30944	0.016	60001045002	2012-08-12	162399	205.00±0.36
8	MCG-6-30-15	203.97378	-34.29554	0.008	60001047003	2013-01-30	127232	120.00±0.31
9	Mkn 335	1.58134	20.20291	0.026	60001041005	2013-06-25	93028	18.00±0.15
10	Mrk 1040	37.06032	31.31166	0.017	60101002004	2015-08-15	64252	69.60±0.34
11	Mrk 110	141.30362	52.28626	0.035	60201025002	2017-01-23	184563	99.24±0.24
12	Mrk 590	33.63984	-0.76669	0.026	90201043002	2016-12-02	51003	5.74±0.11
13	Mrk 766	184.61046	29.81287	0.013	60001048002	2015-01-24	90174	52.30±0.25
14	Swift J2127.4+5654	321.93729	56.94436	0.014	60001110005	2012-11-06	74583	82.28±0.34

the modules. Some sources showed emission features around 6.4 keV. We added a ZGAUSS model component in those sources, with the line energy centred at about 6.4 keV. The width of the emission line  $\sigma$  was set as a free parameter. This resulted in 14 sources in which an improvement in  $\chi^2$  over the power law model was observed on the addition of a broad ZGAUSS ( $\sigma_{\text{brd}} \gtrsim 0.2$  keV). In these sources, the fit statistic improved with an f-test probability  $<0.01$  (significant at  $\sim 99\%$ ) corresponding to a change in  $\chi^2$  greater than 10. As an example, in Fig. 1, we show the residuals of IC 4329A before and after including the redshifted Gaussian component. The broad Fe lines were detected in the sources IC 4329A (Nandra et al. 2007, 1997), Mrk 766 (Nandra et al. 2007, 1997), MCG-6-30-15 (Tanaka et al. 1995; Fabian et al. 2002; Wilms et al. 2001; Miniutti et al. 2007; Nandra et al. 2007), Mrk 1040 (Reynolds et al. 1995), Mrk 335 (Patrick et al. 2011), Ark 120 (Nandra et al. 2007; Nardini et al. 2011) and Fairall 9 (Nandra et al. 1997) based on the data from previous observatories.

Further, an additional ZGUASS was included to check the presence of the narrow ( $\sigma_{\text{nrw}} = 0.001$  keV) Fe K $\alpha$  emission line ( $E_{\text{nrw}}=6.4$  keV) due to neutral reflection. The detection of narrow Fe emission lines by *Chandra* HETG observations was already reported for the sources Fairall 9, MCG-06-30-15 (Yaqoob & Padmanabhan (2004); Lee et al. (2002)), IC 4329A (McKernan & Yaqoob 2004), Ark 120 (Nardini et al. 2016), Mrk 590 (Longinotti et al. 2007) and 3C 382 (Gliozzi et al. 2007). In the present study, it is observed that the spectral data for three among 14 sources provided a better fit statistic on the addition of the new component. So in the final sample, there are 14 sources for which the spectra show the effect of relativistic reflection, and there are three sources in which both relativistic and distant reflection lines are clearly present in the spectra. The details of these sources are given in Table 1, and the best-fit parameters of the three models are given in Table 2, Table 3 & Table 4. See Appendix A for the residual plots for all the sources in the sample fitted with the model TBABS×POWERLAW. The sources have a redshift range of  $0.008 < z < 0.104$ . It is also noted that five sources in the final sample are NLS1 galaxies.

We have also tested the presence of intrinsic absorption in the sources using the model ZTBABS parameterised by

the equivalent hydrogen column  $N_{\text{H}}^{\text{Int}}$ . The fit was improved ( $|\Delta\chi^2| > 10$ ) by the inclusion of the component for 3C 382, IC 4329A and Mrk 110. For other sources in the sample, the statistic has not improved, and the parameter  $N_{\text{H}}^{\text{Int}}$  was not constrained. Hence the intrinsic absorption is included in further modelling for these three sources.

### 3 SPECTRAL MODELLING

Here, we use the model RELXILL (García et al. 2014; Dauser et al. 2014) that provides a proper treatment of the relativistic reflection near strong gravitational fields of SMBH. The relativistic reflection code RELXILL takes care of the angle dependent reflection spectrum, and is a combination of the models RELCONV and XILLVER. RELCONV is the convolution model for RELLINE<sup>4</sup> code (Dauser et al. 2010) that is used to calculate the relativistic smearing of reflected radiation. The angle-dependent reflection code XILLVER (García & Kallman (2010); García et al. (2011)) gives the X-ray reflected spectrum emerging from the surface of an illuminated accretion disc. The code calculates proper reflected spectrum for each point in the disc by solving the equations of radiative transfer, energy balance, and ionisation equilibrium in a Compton-thick, plane-parallel medium. The ionisation balance at each point is calculated using the photoionisation code XSTAR (Kallman & Bautista (2001)).

In order to model the broad Fe line and the other spectral components, we used the local model RELXILL (version 0.4c) considering the relativistic reflection in coronal geometry. The model includes both the primary continuum irradiating the accretion disc and the reflection combined with relativistic smearing. The basic parameters of this model are the indices ( $\beta 1$  &  $\beta 2$ ) of the power law disc emissivity profile, break radius ( $R_{\text{br}}$ ) where emissivity profile changes from  $\beta 1$  to  $\beta 2$ , black hole spin  $a$ , inclination with respect to the normal to the disc  $i$ , inner and outer radii of disc  $R_{\text{in}}$  &  $R_{\text{out}}$ , ionisation parameter  $\xi$  of the accretion disc, iron abundance  $A_{\text{Fe}}$  (in units of solar abundance) of material in the disc,

<sup>4</sup> See the website <http://www.sternwarte.uni-erlangen.de/~dauser/research/relline/> for more details of RELLINE.

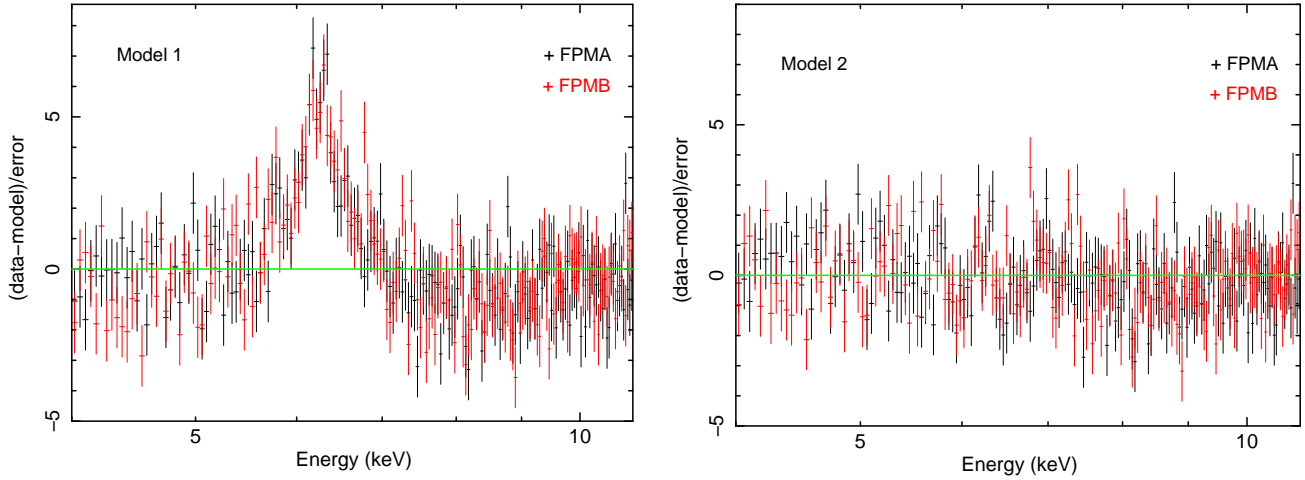


**Figure 1.** Deviations of the observed data from the best-fitting Model 1: CONSTANT $\times$ TBABS $\times$ POWERLAW and Model 2: CONSTANT $\times$ TBABS(zGAUSS + POWERLAW) for IC 4329A. Left: The excess emission around  $\sim 5 - 8$  keV showing the presence of broad iron line component. Right: The residuals from the spectral fit after the inclusion of a broad zGAUSS component. FPMA data are plotted in black colour, and FPMB data are plotted in red colour.

**Table 2.** Best-fit parameters of sample fitted with *NuSTAR* data using the absorbed power law model. The power law normalisation  $N_{\text{pow}}$  is in units of photons  $\text{keV}^{-1}\text{cm}^{-2}\text{s}^{-1}$ .

No.	Object	$N_{\text{H}}^{\text{Gal}}$ $10^{20}\text{cm}^{-2}$	$\Gamma$	$N_{\text{pow}}$ $10^{-2}$	$\chi^2/\text{dof}$
1	3C 382	6.98	$1.732 \pm 0.008$	$0.76 \pm 0.01$	762.49/672
2	4C 74.26	11.60	$1.763 \pm 0.008$	$0.78 \pm 0.01$	925.37/669
3	Ark 120	9.78	$1.863 \pm 0.012$	$12.92_{-0.37}^{+0.38}$	918.55/552
4	Ark 564	5.34	$2.595 \pm 0.010$	$18.00 \pm 0.35$	1098.93/657
5	ESO 141-G 055	4.83	$1.795 \pm 0.009$	$0.73_{-0.01}^{+0.02}$	885.54/640
6	Fairall 9	3.16	$1.826 \pm 0.010$	$6.61 \pm 0.14$	878.14/597
7	IC 4329A	4.61	$1.714 \pm 0.004$	$26.68 \pm 0.27$	2162.95/1342
8	MCG-6-30-15	3.92	$1.932 \pm 0.006$	$1.71 \pm 0.02$	1899.32/884
9	Mkn 335	3.56	$1.679_{-0.019}^{+0.020}$	$0.15 \pm 0.01$	711.21/273
10	Mrk 1040	6.63	$1.751 \pm 0.011$	$7.06 \pm 0.17$	801.90/583
11	Mrk 110	1.30	$1.812 \pm 0.007$	$1.16 \pm 0.02$	598.37/493
12	Mrk 590	2.65	$1.655_{-0.043}^{+0.044}$	$0.72 \pm 0.07$	224.25/203
13	Mrk 766	1.78	$2.011 \pm 0.011$	$8.89 \pm 0.21$	799.75/532
14	Swift J2127.4+5654	76.50	$1.827 \pm 0.009$	$0.98 \pm 0.02$	1091.96/638

Note: dof - degrees of freedom

**Table 3.** Best-fit parameters of broad Gaussian and power law models.  $E_{\text{brd}}$ ,  $\sigma_{\text{brd}}$  and  $N_{\text{brd}}$  are the line energy, width and normalisation of the broad Gaussian component. The units for  $N_{\text{pow}}$  and  $N_{\text{brd}}$  are photons  $\text{keV}^{-1}\text{cm}^{-2}\text{s}^{-1}$  and photons  $\text{cm}^{-2}\text{s}^{-1}$ , respectively.

No.	Object	$\Gamma$	$N_{\text{pow}}$ $10^{-2}$	$E_{\text{brd}}$ keV	$\sigma_{\text{brd}}$ keV	$N_{\text{brd}}$ $10^{-5}$	$\chi^2/\text{dof}$
1	3C 382	$1.721 \pm 0.009$	$0.74 \pm 0.02$	$6.35 \pm 0.11$	$0.43_{-0.13}^{+0.16}$	$4.28_{-0.95}^{+1.10}$	673.49/669
2	4C 74.26	$1.748 \pm 0.009$	$0.74 \pm 0.02$	$6.26 \pm 0.11$	$0.44_{-0.10}^{+0.11}$	$5.17_{-1.00}^{+1.10}$	815.20/666
3	Ark 120	$1.849 \pm 0.009$	$1.23 \pm 0.02$	$6.36 \pm 0.04$	$0.23 \pm 0.06$	$7.00_{-0.93}^{+0.97}$	807.09/649
4	Ark 564	$2.585_{-0.015}^{+0.013}$	$1.66_{-0.06}^{+0.05}$	$5.87_{-0.30}^{+0.22}$	$1.30_{-0.18}^{+0.22}$	$9.51_{-1.76}^{+2.61}$	688.08/654
5	ESO 141-G 055	$1.786 \pm 0.010$	$0.71_{-0.01}^{+0.02}$	$6.34_{-0.07}^{+0.08}$	$0.26_{-0.12}^{+0.10}$	$3.08 \pm 0.69$	788.76/637
6	Fairall 9	$1.811 \pm 0.010$	$0.63 \pm 0.01$	$6.33_{-0.05}^{+0.04}$	$0.25_{-0.06}^{+0.06}$	$4.58_{-1.59}^{+0.62}$	640.62/594
7	IC 4329A	$1.685 \pm 0.003$	$2.46 \pm 0.02$	$6.37 \pm 0.03$	$0.27 \pm 0.04$	$12.81_{-1.05}^{+1.08}$	1708.03/1339
8	MCG-6-30-15	$1.913_{-0.009}^{+0.008}$	$1.61_{-0.04}^{+0.03}$	$5.94_{-0.21}^{+0.16}$	$0.65_{-0.14}^{+0.17}$	$11.32_{-2.13}^{+3.03}$	1523.16/881
9	Mkn 335	$1.424_{-0.038}^{+0.037}$	$0.08 \pm 0.01$	$4.35_{-0.31}^{+0.24}$	$1.42_{-0.15}^{+0.19}$	$16.62_{-3.07}^{+4.10}$	428.21/270
10	Mrk 1040	$1.739 \pm 0.012$	$0.68 \pm 0.02$	$6.38_{-0.10}^{+0.08}$	$0.36_{-0.09}^{+0.11}$	$4.93_{-0.89}^{+1.01}$	669.02/580
11	Mrk 110	$1.807_{-0.008}^{+0.007}$	$1.13 \pm 0.02$	$6.37 \pm 0.10$	$0.33_{-0.14}^{+0.14}$	$3.37_{-0.81}^{+1.92}$	531.55/490
12	Mrk 590	$1.624 \pm 0.047$	$0.07 \pm 0.01$	$6.40 \pm 0.16$	$0.39_{-0.13}^{+0.16}$	$1.38_{-0.42}^{+0.42}$	188.98/200
13	Mrk 766	$2.005 \pm 0.012$	$0.87 \pm 0.02$	$6.37_{-0.17}^{+0.16}$	$0.43 \pm 0.13$	$2.49_{-0.68}^{+0.71}$	745.02/529
14	Swift J2127.4+5654	$1.820 \pm 0.009$	$0.96 \pm 0.02$	$6.37 \pm 0.07$	$0.24_{-0.08}^{+0.09}$	$3.71_{-0.73}^{+0.79}$	988.84/635

**Table 4.** Best-fit parameters of the model with an additional narrow Gaussian component.  $E_{\text{brd}}$  &  $N_{\text{brd}}$  are the line energy and normalisation of the broad Gaussian, and  $N_{\text{nrw}}$  is the normalisation of the narrow Gaussian component.  $E_{\text{nrw}}$  &  $\sigma_{\text{nrw}}$  are frozen to 6.4 keV and  $10^{-3}$  keV respectively.  $N_{\text{pow}}$  is in units of photons  $\text{keV}^{-1}\text{cm}^{-2}\text{s}^{-1}$  and  $N_{\text{brd}}$  &  $N_{\text{nrw}}$  are in units of photons  $\text{cm}^{-2}\text{s}^{-1}$ .

No.	Object	$\Gamma$	$N_{\text{pow}}$	$E_{\text{brd}}$	$\sigma_{\text{brd}}$	$N_{\text{brd}}$	$N_{\text{nrw}}$	$\chi^2/\text{dof}$
								$10^{-2}$
				keV	keV	$10^{-5}$	$10^{-5}$	
1	3C 382	$1.721 \pm 0.009$	$0.74 \pm 0.02$	$6.34^{+0.17}_{-0.19}$	$0.53^{+0.32}_{-0.19}$	$3.88^{+1.30}_{-1.26}$	$< 1.39$	672.40/668
2	4C 74.26	$1.748 \pm 0.009$	$0.74 \pm 0.02$	$6.24^{+0.12}_{-0.16}$	$0.46^{+0.15}_{-0.10}$	$4.93^{+1.18}_{-1.33}$	$< 1.17$	814.97/665
3	Ark 120	$1.847^{+0.009}_{-0.010}$	$1.23 \pm 0.03$	$6.27^{+0.12}_{-0.41}$	$0.37^{+0.30}_{-0.14}$	$4.95^{+1.89}_{-1.63}$	$2.54^{+1.64}_{-2.06}$	803.34/648
4	Ark 564	$2.583^{+0.014}_{-0.017}$	$1.65^{+0.06}_{-0.07}$	$5.75^{+0.28}_{-0.33}$	$1.40^{+0.22}_{-0.17}$	$10.02^{+3.46}_{-3.07}$	$0.25 \pm 0.25$	685.31/653
5	ESO 141-G 055	$1.786 \pm 0.010$	$0.71^{+0.02}_{-0.01}$	$6.34^{+0.09}_{-0.10}$	$0.25^{+0.17}_{-0.12}$	$3.09^{+0.68}_{-1.22}$	$< 1.08$	788.76/636
6	Fairall 9	$1.779 \pm 0.014$	$0.58 \pm 0.02$	$5.00^{+0.55}_{-1.10}$	$1.21^{+0.15}_{-0.16}$	$8.57^{+2.50}_{-5.23}$	$2.62 \pm 0.40$	639.40/593
7	IC 4329A*	$1.684 \pm 0.003$	$2.45 \pm 0.02$	$6.32^{+0.07}_{-0.08}$	$0.45^{+0.10}_{-0.09}$	$9.80 \pm 1.57$	$4.31^{+1.13}_{-1.27}$	1687.22/1338
8	MCG-6-30-15*	$1.885 \pm 0.008$	$1.49 \pm 0.03$	$< 5.03$	$1.14 \pm 0.08$	$20.77^{+2.82}_{-2.65}$	$2.99 \pm 0.45$	1394.95/880
9	Mkn 335*	$1.517^{+0.029}_{-0.028}$	$0.10 \pm 0.01$	$< 5.02$	$0.92^{+0.08}_{-0.11}$	$7.69^{+1.05}_{-1.20}$	$0.88 \pm 0.24$	408.01/269
10	Mrk 1040	$1.704^{+0.016}_{-0.015}$	$0.62^{+0.03}_{-0.01}$	$< 5.24$	$1.35^{+0.18}_{-0.19}$	$11.63^{+3.62}_{-3.34}$	$2.10^{+0.47}_{-0.49}$	663.36/579
11	Mrk 110	$1.807 \pm 0.007$	$1.13 \pm 0.02$	$6.37^{+0.12}_{-0.14}$	$0.33^{+0.25}_{-0.10}$	$3.37^{+0.86}_{-1.28}$	$< 1.05$	531.55/489
12	Mrk 590	$1.624^{+0.047}_{-0.046}$	$0.07 \pm 0.01$	$6.40^{+0.24}_{-0.18}$	$0.40^{+0.21}_{-0.13}$	$1.36^{+0.48}_{-0.69}$	$< 0.50$	188.96/199
13	Mrk 766	$2.005 \pm 0.012$	$0.87 \pm 0.02$	$6.37^{+0.16}_{-0.19}$	$0.42^{+0.15}_{-0.10}$	$2.48^{+0.72}_{-0.80}$	$< 0.46$	745.00/528
14	Swift J2127.4+5654	$1.819^{+0.010}_{-0.009}$	$0.96 \pm 0.02$	$6.34^{+0.11}_{-0.41}$	$0.31^{+0.26}_{-0.16}$	$3.05^{+0.75}_{-1.44}$	$< 2.12$	988.43/634

Note: \*Sources showing  $|\Delta\chi^2| > 10$  on the addition of a narrow Gaussian.

photon index  $\Gamma$  & high energy cut-off  $E_{\text{cut}}$  of the incident power law spectrum, redshift  $z$  of the source, reflection fraction  $R_f$ , and normalisation  $N_{\text{relxill}}$ <sup>5</sup>. The implementation of relativistic reflection fraction  $R_f$ , a quantity independent of inclination and the condition of the reflector, is a major advantage of RELXILL. The relativistic reflection fraction is defined as the ratio of the coronal intensity that irradiates the disc to the coronal intensity that directly reaches the observer (Dauser et al. (2016)). Unlike other reflection models (e.g. PEXRAV), RELXILL considers the light-bending effects near the black hole.

In the three sources where significant narrow Fe emission lines were detected (see Sec. 2.1), we incorporated a XILLVER component in addition to RELXILL. For this additional XILLVER component, the value of  $\log \xi$  was fixed at 0. This will ensure the effect of reflection from distant material resulting in neutral narrow Fe K $\alpha$  emission. The other parameters characterising the model are  $\Gamma$ ,  $A_{\text{Fe}}$ ,  $E_{\text{cut}}$ ,  $i$ ,  $z$  and normalisation  $N_{\text{xillver}}$ . Thus, to model the relativistic reflection spectrum, RELXILL was used and XILLVER was included to model the distant reflection.

To simplify the spectral fitting, many parameters were frozen. Assuming that there is no break radius in the emissivity profile, the emissivity indices ( $\beta_1$  and  $\beta_2$ ) were always tied together, where  $\beta_1$  was free to vary. We fixed the break and outer radii to the model default values of  $15 R_g$  and  $400 R_g$ , respectively. The inclination was set to  $30^\circ$  which is adequate for type 1 Seyferts. The spectra were fitted for different values of black hole spins, assuming that  $R_{\text{in}}$  extends down to the innermost stable circular orbit  $R_{\text{ISCO}}$ . Whenever the spectrum was fit with both RELXILL and XILLVER, the parameters  $\Gamma$ ,  $A_{\text{Fe}}$ ,  $E_{\text{cut}}$  and  $i$  in the model components were tied.

<sup>5</sup> The normalisations of RELXILL and XILLVER models are defined in Appendix A of Dauser et al. (2016).

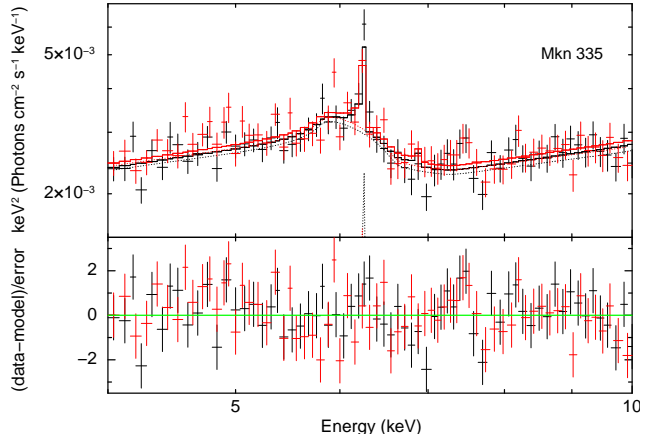


**Figure 2.** Broadband X-ray spectral fit of Mkn 335 using the models RELXILL and XILLVER with spin 0 (shown in the 4–10 keV band). The upper panel shows the unfolded spectra and the best-fit model and the lower panel shows the residuals, showing narrow absorption features above  $\sim 6$  keV.

### 3.1 Fe K absorption

The presence of blue-shifted narrow absorption lines associated with the FeXXV–XXVI K-shell transitions have been detected in the  $\sim 7$  –  $10$  keV band of AGN. These features are identified with the absorption from highly ionised circumnuclear gas outflowing with velocities up to  $0.2$  –  $0.4c$ . A detailed search for the evidence of such ultra-fast outflows (UFOs) in the  $7$  –  $10$  keV band in a sample of radio-quiet AGN was carried out by Tombesi et al. (2010). They detected blue-shifted Fe K absorption lines in *XMM-Newton* spectra of the sources, and modelled these lines with inverted Gaussian components by fixing the width at 10 eV or 100 eV (see Table A2 in Tombesi et al. (2010)). They found that the corresponding outflow velocities of these blue-shifted lines range from zero to  $\sim 0.3c$ . Their sample included nine sources in our sample. They observed single or multiple Fe K-shell

absorption lines in IC 4329A ( $E_{\text{rest}} \sim 7.69$  keV, width=100 eV), Ark 120 ( $E_{\text{rest}} \sim 9.18$  keV, width=10 eV), Mrk 766 ( $E_{\text{rest}} \sim 7.28$  keV, width=100 eV;  $E_{\text{rest}} \sim 7.63$  keV, width=10 eV) and no significant absorption was detected in MCG-6-30-15, Mrk 110, Fairall 9, Mkn 335, Mrk 590 and Ark 564. In a further study, Tombesi et al. (2011) presented detailed modelling of these highly ionised absorbers using XSTAR and obtained outflow velocities of  $\sim 0.097c$  for IC 4329A,  $\sim 0.306c$  for Ark 120 and  $\sim 0.082c$ (0.088c) for Mrk 766. Markowitz et al. (2006) also found a narrow absorption feature in the *XMM-Newton* spectrum of IC 4329A, around 7.7 keV, which is an evidence for a high velocity ( $\sim 0.1c$ ) outflow in the source. Gofford et al. (2013) performed a search for the Fe K absorption lines in the *Suzaku* spectra of AGN. They reported highly ionised outflow features with velocities of 0.185c, 0.231c, 0.007c and 0.061c, respectively in 4C +74.26, SWIFT J2127.4+5654, MCG-6-30-15 and Mrk 766. In Ark 564, Papadakis et al. (2007) detected highly ionised absorption line at  $\sim 8.14$  keV in the *XMM-Newton* EPIC-PN spectrum, probably corresponding to the FeXXVI-K $\alpha$ , indicating the presence of outflowing material with a velocity of  $\sim 0.17c$ . However, Mizumoto et al. (2019) reported no absorption line in Ark 564, indicating a face-on geometry of the wind. Mkn 335 has been identified with ionised absorption features in the Fe K band in *XMM-Newton* and *NuSTAR* spectra (Gallo et al. 2019; Longinotti et al. 2019; Parker et al. 2014). Gallo et al. (2019) observed highly ionised absorption lines in Mkn 335 which could be attributed to accretion disc winds outflowing with a velocity of  $\sim 0.12c$ .

Although the Fe K absorption features are reported to be present in the *XMM-Newton* and/or *Suzaku* spectra of most of the sources in the present sample, these narrow lines may not be detected in the low-resolution *NuSTAR* spectra. However, we examined the spectra of the sources in the  $\sim 6$ –10 keV band to identify the presence of Fe K absorption line. The spectrum of Mkn 335 showed narrow absorption lines above  $\sim 6$  keV which could be related to the ultra-fast outflows (see Fig. 2). We then included the analytic model WARMABS to model the outflow features, instead of using XSTAR MTABLES. The model gives the absorber column density, ionisation parameter, element abundances in the solar unit, turbulent velocity and redshift of the outflowing gas. Despite the absorption profiles were found to be modelled, the addition of WARMABS did not improve the fit significantly over RELXILL+XILLVER model. Moreover, the observed redshift of the absorber corresponds to an outflow velocity of  $\sim 4000$  km s $^{-1}$ , which is less than the expected velocity for an ultra-fast outflow. It should also be noted that the best-fit reflection fraction and photon index for this model lie within the range obtained earlier, with lower mean values.

## 4 RESULTS & DISCUSSION

The present work determines the relativistic reflection fraction of a sample of 14 type 1 Seyferts observed with *NuSTAR*. In this sample, the spectra of 11 sources were modelled with RELXILL, and those of three sources with a combination of RELXILL and XILLVER. We fitted the spectra with the same model for spin parameters of 0 and 0.998. For both the spin parameters, the photon index and reflection frac-

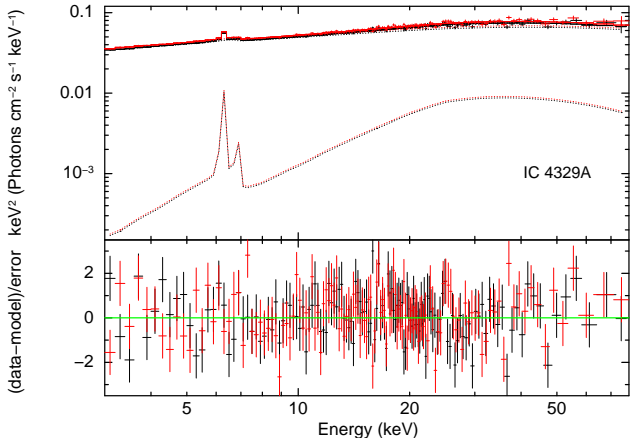


**Figure 3.** Broadband X-ray (3 – 79 keV) spectra of IC 4329A fitted with the models RELXILL and XILLVER for spin 0. The upper panel shows the unfolded spectra and the best-fit models while the lower panel shows the residuals for the spectral fit.

tion were well constrained for all the sources. The values of  $R_f$  obtained for these sources are roughly in the range of 0.1 – 3.8, with a mean value of around 0.9 for  $a = 0$ . For  $a = 0.998$ ,  $R_f$  ranges from  $\sim 0.1$  to  $\sim 4.9$  and has a mean value of  $\sim 0.98$ . However, we find that both the reflection fraction and the photon index are consistent within errorbars for non-rotating ( $a = 0$ ) and maximally rotating ( $a = 0.998$ ) black holes. The obtained reflection fraction is similar to the previous results from Burlon et al. (2011) and Ballantyne (2014) and higher than the values reported by Del Moro et al. (2017) and Ricci et al. (2011). However, the inconsistency in the values of reflection fraction may be attributed to the different models used in the analysis. The above mentioned studies used PEXRAV and PEXMON models for describing the reflection component while the present work used RELXILL model.

A summary of the broadband spectral analysis of these sources are given in Table 5 and Table 6. The broadband spectral fitting plot for IC 4329A using the model CONSTANT $\times$ TBABS $\times$ ZTBABS(=RELXILL + XILLVER) is shown in Fig. 3. The spectral fit and residuals for the final model for the whole sample are given in Appendix B.

### 4.1 Correlations

We obtained the correlations between the relativistic reflection fraction and the photon index in our sample using Spearman's rank-order method Press et al. (1992). A significant positive correlation is observed between  $R_f$  and  $\Gamma$  with a rank of 0.83 and p-value of 0.0003 for  $a = 0$ . A similar trend is observed for  $a = 0.998$  as well with a rank of 0.65 and a p-value of 0.01. The parameters for different spin values are plotted in Fig. 4. Pearson's correlation also shows a weak positive linear trend between  $\log R_f$  and  $\Gamma$  with a null hypothesis probability (p-value) of 0.05 and a rank of 0.54 for  $a=0$ . We have also checked the correlations between other parameters such as X-ray luminosity, X-ray Eddington ratio, Fe abundance, ionisation parameter and high energy cut-off. However, we did not find any significant correlations among these parameters.

**Table 5.** Best-fit parameters of the models CONSTANT $\times$ TBABS $\times$ RELXILL and/or CONSTANT $\times$ TBABS(REFXILL+XILLVER) for inclination  $i=30^\circ$  & spin  $a=0$ .  $\Gamma$ : hard X-ray photon index,  $\beta 1$ : emissivity index,  $\log \xi$ : logarithm of ionisation parameter,  $A_{\text{Fe}}$ : iron abundance in solar units,  $E_{\text{cut}}$ : cut-off energy in keV,  $R_f$ : reflection fraction,  $N_{\text{relxill}}$ : Normalisation of RELXILL,  $N_{\text{xillver}}$ : Normalisation of XILLVER.

No.	Object	$N_{\text{H}}^{\text{Int}}$	$\Gamma$	$E_{\text{cut}}$	$R_f$	$\beta 1$	$\log \xi$	$A_{\text{Fe}}$	$N_{\text{relxill}}$	$N_{\text{xillver}}$	$\chi^2/\text{dof}$
		$10^{20} \text{ cm}^{-2}$		keV					$10^{-4}$	$10^{-5}$	
1	3C 382	$36.34^{+35.55}_{-22.81}$	$1.67 \pm 0.05$	$132.75^{+98.32}_{-39.98}$	$0.13^{+0.07}_{-0.03}$	$< 2.19$	$< 2.13$	$> 4.37$	$1.71^{+0.27}_{-0.17}$		650.07/666
2	4C 74.26		$1.81^{+0.05}_{-0.06}$	$155.64^{+49.05}_{-48.21}$	$0.58 \pm 0.16$	$2.46^{+0.57}_{-0.43}$	$2.70^{+0.06}_{-0.35}$	$0.93^{+1.30}_{-0.27}$	$1.34^{+0.08}_{-0.09}$		696.34/664
3	Ark 120		$1.97 \pm 0.03$	$393.17^{+497.82}_{-152.75}$	$0.61^{+0.04}_{-0.10}$	$< 1.52$	$< 1.07$	$2.43^{+0.60}_{-0.57}$	$2.36^{+0.21}_{-0.15}$		693.41/647
4	Ark 564		$2.31^{+0.04}_{-0.06}$	$59.00^{+14.82}_{-11.84}$	$0.59^{+0.30}_{-0.29}$	$< 1.96$	$> 4.27$	$3.57^{+3.33}_{-1.75}$	$0.73^{+0.31}_{-0.23}$		644.43/652
5	ESO 141-G 055		$1.92^{+0.03}_{-0.02}$	$> 450.58$	$0.53^{+0.04}_{-0.11}$	$< 1.31$	$< 2.02$	$1.58^{+0.90}_{-0.55}$	$1.72^{+0.06}_{-0.16}$		669.75/635
6	Fairall 9		$1.92 \pm 0.04$	$349.25^{+381.40}_{-139.91}$	$0.65^{+0.17}_{-0.17}$	$1.37^{+0.57}_{-0.57}$	$< 1.09$	$2.97^{+0.55}_{-0.64}$	$1.27^{+0.13}_{-0.10}$		548.62/592
7	IC 4329A	$< 42.82$	$1.69 \pm 0.03$	$153.94^{+24.85}_{-24.37}$	$0.12^{+0.04}_{-0.05}$	$2.48^{+0.88}_{-0.59}$	$2.68^{+0.11}_{-0.29}$	$2.80^{+0.50}_{-0.75}$	$6.11^{+0.28}_{-0.26}$	$4.58^{+1.46}_{-0.96}$	1442.41/1335
8	MCG-6-30-15		$2.06 \pm 0.02$	$149.73^{+31.15}_{-12.46}$	$1.04^{+0.12}_{-0.18}$	$2.98^{+0.40}_{-0.33}$	$1.69^{+0.07}_{-0.22}$	$2.51^{+0.34}_{-0.36}$	$2.46^{+0.07}_{-0.03}$	$1.31^{+0.52}_{-0.87}$	933.30/878
9	Mkn 335		$2.15^{+0.10}_{-0.02}$	$> 194.58$	$3.75^{+0.83}_{-0.21}$	$5.32^{+2.05}_{-0.98}$	$< 2.35$	$2.36^{+0.82}_{-0.41}$	$0.29 \pm 0.02$	$0.57^{+0.48}_{-0.51}$	267.92/267
10	Mrk1040		$1.83^{+0.03}_{-0.02}$	$> 359.01$	$0.52^{+0.13}_{-0.10}$	$2.23^{+0.49}_{-0.64}$	$2.76^{+0.13}_{-0.45}$	$2.71^{+1.21}_{-1.11}$	$1.75^{+0.13}_{-0.23}$		581.81/578
11	Mrk 110	$62.48^{+43.30}_{-28.46}$	$1.83^{+0.07}_{-0.05}$	$219.30^{+437.39}_{-112.36}$	$0.16^{+0.07}_{-0.10}$	$< 2.35$	$2.70^{+0.06}_{-0.93}$	$< 6.54$	$2.30^{+0.39}_{-0.18}$		510.46/487
12	Mrk 590		$1.64^{+0.16}_{-0.12}$	$> 54.68$	$0.51^{+0.21}_{-0.20}$	$< 2.38$	$< 2.95$	$> 2.17$	$0.19^{+0.12}_{-0.04}$		191.93/198
13	Mrk 766		$2.24^{+0.06}_{-0.02}$	$> 455.64$	$1.06 \pm 0.19$	$1.87^{+0.48}_{-0.69}$	$< 2.42$	$0.90^{+0.16}_{-0.14}$	$1.47 \pm 0.07$		558.97/527
14	Swift J2127.4+5654		$2.13^{+0.07}_{-0.08}$	$138.0^{+94.52}_{-39.64}$	$1.78^{+0.81}_{-0.44}$	$1.86^{+0.45}_{-0.43}$	$1.77^{+0.24}_{-0.38}$	$< 0.67$	$1.58^{+0.08}_{-0.07}$		664.01/633

**Table 6.** Best-fit parameters of the models CONSTANT $\times$ TBABS $\times$ RELXILL and CONSTANT $\times$ TBABS(REFXILL+XILLVER) for  $i = 30^\circ$  &  $a = 0.998$ .  $\Gamma$ : hard X-ray photon index,  $\beta 1$ : emissivity index,  $\log \xi$ : logarithm of ionisation parameter,  $A_{\text{Fe}}$ : iron abundance in solar units,  $E_{\text{cut}}$ : cut-off energy in keV,  $R_f$ : reflection fraction,  $N_{\text{relxill}}$ : Normalisation of RELXILL,  $N_{\text{xillver}}$ : Normalisation of XILLVER.

No.	Object	$N_{\text{H}}^{\text{Int}}$	$\Gamma$	$E_{\text{cut}}$	$R_f$	$\beta 1$	$\log \xi$	$A_{\text{Fe}}$	$N_{\text{relxill}}$	$N_{\text{xillver}}$	$\chi^2/\text{dof}$
		$10^{20} \text{ cm}^{-2}$		keV					$10^{-4}$	$10^{-5}$	
1	3C 382	$36.62^{+54.12}_{-35.78}$	$1.67^{+0.05}_{-0.06}$	$132.78^{+99.90}_{-38.44}$	$0.13^{+0.07}_{-0.03}$	$< 2.00$	$< 2.14$	$> 4.39$	$1.71^{+0.28}_{-0.17}$		650.13/666
2	4C 74.26		$1.80 \pm 0.05$	$154.11^{+55.68}_{-44.28}$	$0.61 \pm 0.16$	$2.32^{+0.32}_{-0.37}$	$2.69^{+0.06}_{-0.35}$	$1.39^{+0.84}_{-0.67}$	$1.35 \pm 0.08$		696.51/664
3	Ark 120		$1.97 \pm 0.03$	$393.61^{+493.76}_{-153.24}$	$0.62^{+0.10}_{-0.12}$	$< 1.52$	$< 1.07$	$2.44^{+0.65}_{-0.57}$	$2.36^{+0.21}_{-0.16}$		693.28/647
4	Ark 564		$2.31^{+0.05}_{-0.06}$	$59.00^{+14.12}_{-11.36}$	$0.59^{+0.10}_{-0.23}$	$< 1.91$	$> 4.27$	$3.57^{+3.31}_{-1.94}$	$0.73^{+0.31}_{-0.24}$		644.43/652
5	ESO 141-G 055		$1.92 \pm 0.03$	$> 446.04$	$0.52^{+0.08}_{-0.06}$	$< 1.33$	$< 2.02$	$1.58^{+0.55}_{-0.55}$	$1.72^{+0.25}_{-0.08}$		669.78/635
6	Fairall 9		$1.92 \pm 0.04$	$336.75^{+376.61}_{-128.54}$	$0.66^{+0.13}_{-0.14}$	$1.44^{+0.49}_{-1.20}$	$< 1.08$	$3.03^{+0.76}_{-0.67}$	$1.27^{+0.13}_{-0.10}$		548.35/592
7	IC 4329A	$< 40.77$	$1.70^{+0.03}_{-0.04}$	$156.89^{+30.64}_{-27.66}$	$0.13 \pm 0.05$	$2.32^{+0.64}_{-0.44}$	$2.69^{+0.20}_{-0.30}$	$2.83^{+1.02}_{-0.69}$	$6.11^{+0.25}_{-0.29}$	$4.64^{+1.30}_{-1.10}$	1441.44/1335
8	MCG-6-30-15		$2.07 \pm 0.03$	$160.02^{+28.76}_{-18.26}$	$1.25^{+0.17}_{-0.26}$	$2.53^{+0.26}_{-0.45}$	$1.69^{+0.07}_{-0.56}$	$2.94^{+0.54}_{-0.63}$	$2.45 \pm 0.07$	$< 1.33$	938.16/7878
9	Mkn 335		$1.87^{+0.26}_{-0.18}$	$128.94^{+732.96}_{-57.63}$	$4.85^{+4.45}_{-4.45}$	$3.97^{+0.50}_{-0.47}$	$2.32^{+0.56}_{-0.56}$	$> 3.76$	$0.22 \pm 0.03$	$0.35 \pm 0.42$	262.83/267
10	Mrk 1040		$1.83^{+0.02}_{-0.02}$	$> 355.73$	$0.56^{+0.15}_{-0.12}$	$2.11^{+0.35}_{-0.55}$	$2.77^{+0.15}_{-0.34}$	$2.91^{+1.39}_{-1.22}$	$1.73^{+0.21}_{-0.23}$		581.85/578
11	Mrk 110	$62.43^{+43.99}_{-19.96}$	$1.83^{+0.07}_{-0.08}$	$219.30^{+412.27}_{-113.95}$	$0.16^{+0.11}_{-0.07}$	$< 2.26$	$< 2.75$	$< 3.57$	$2.30^{+0.39}_{-0.18}$		510.48/487
12	Mrk 590		$1.62^{+0.19}_{-0.12}$	$> 53.41$	$0.49^{+0.29}_{-0.18}$	$< 2.18$	$< 2.66$	$> 1.39$	$0.18^{+0.13}_{-0.04}$		192.10/198
13	Mrk 766		$2.28^{+0.07}_{-0.06}$	$> 354.63$	$1.26^{+0.20}_{-0.23}$	$< 1.91$	$1.69^{+0.08}_{-0.17}$	$0.71^{+0.16}_{-0.14}$	$1.47^{+0.08}_{-0.09}$		549.90/527
14	Swift J2127.4+5654		$2.14^{+0.08}_{-0.10}$	$126.75^{+36.55}_{-34.99}$	$1.86^{+1.10}_{-0.48}$	$1.66^{+0.41}_{-0.77}$	$1.58^{+0.44}_{-0.22}$	$< 0.72$	$1.60 \pm 0.12$		664.73/633

Many previous works have studied the dependence of Compton reflection on the hard X-ray spectral slope in AGN (e.g. Zdziarski et al. (1999); Beloborodov (1999); Malzac et al. (2001); Mattson et al. (2007); Dadina (2008); Molina et al. (2009); Boissay et al. (2016); Del Moro et al. (2017); Zappacosta et al. (2018)). Zdziarski et al. (1999) found a significant correlation between the relative strength of Compton reflection (defined as  $\Omega/2\pi$ ;  $\Omega$  is the solid angle subtended by the reflector) and  $\Gamma$ , in their sample of Seyferts. They argued that an internal feedback mechanism, where the medium emitting seed photons for the primary X-ray emission also serves as the medium for reflection, is responsible for the observed correlation. Mattson et al. (2007), though observed a strong correlation between the relative amount of reflection and photon index in a sample of RXTE-observed Seyfert 1 and 1.2 galaxies, ruled out any physical relevance arguing that it is due to the presence of

model degeneracies. Dadina (2008) found a significant correlation between the relative amount of reflection and the photon index in a sample of Seyfert galaxies in the local Universe ( $z \leq 0.1$ ). Contrary to this, Molina et al. (2009) did not observe any correlation between reflection fraction and  $\Gamma$  in a sample of type 1 AGN observed with INTEGRAL. Another study by Lubiński et al. (2016) on the hard X-ray spectra of an INTEGRAL sample of 28 Seyfert galaxies, together with the X-ray data from XMM-Newton, Suzaku and RXTE, reported a less prominent correlation between the reflection strength and the photon index. Here, using the better quality data from NuSTAR, we further confirm the  $R_f - \Gamma$  correlation in our sample of Seyfert 1s. Recently, Panagiotou & Walter (2019) studied the NuSTAR sample of local AGN by classifying the sources based on X-ray spectral shape. They obtained an average reflection strength (measure of Compton hump intensity with respect to pri-

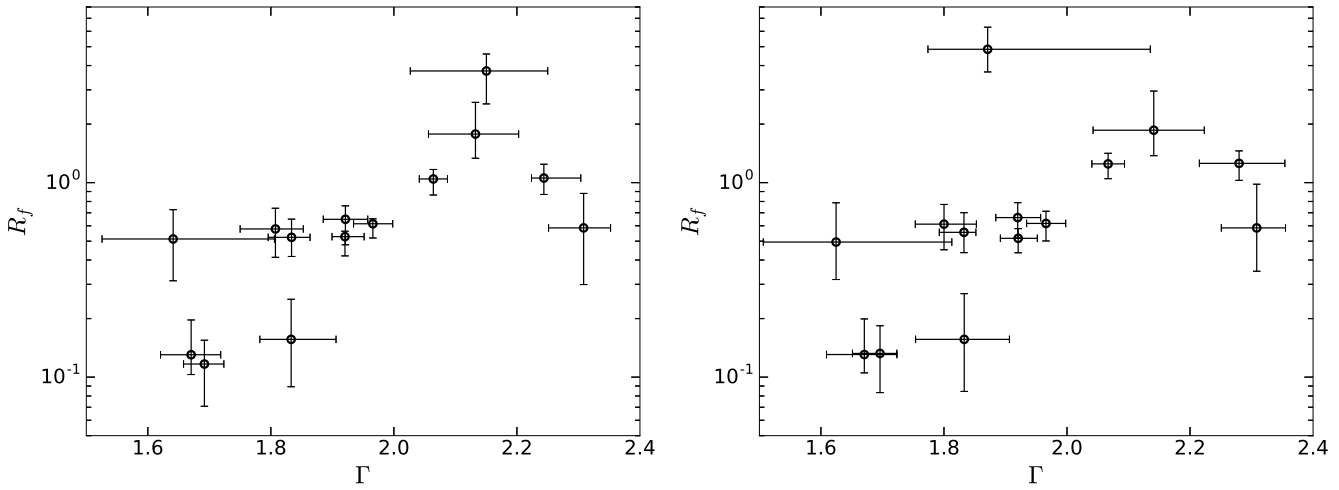


**Figure 4.** Relationship between  $R_f$  and  $\Gamma$  for the sample for  $a=0$  (left) and  $a=0.998$  (right).

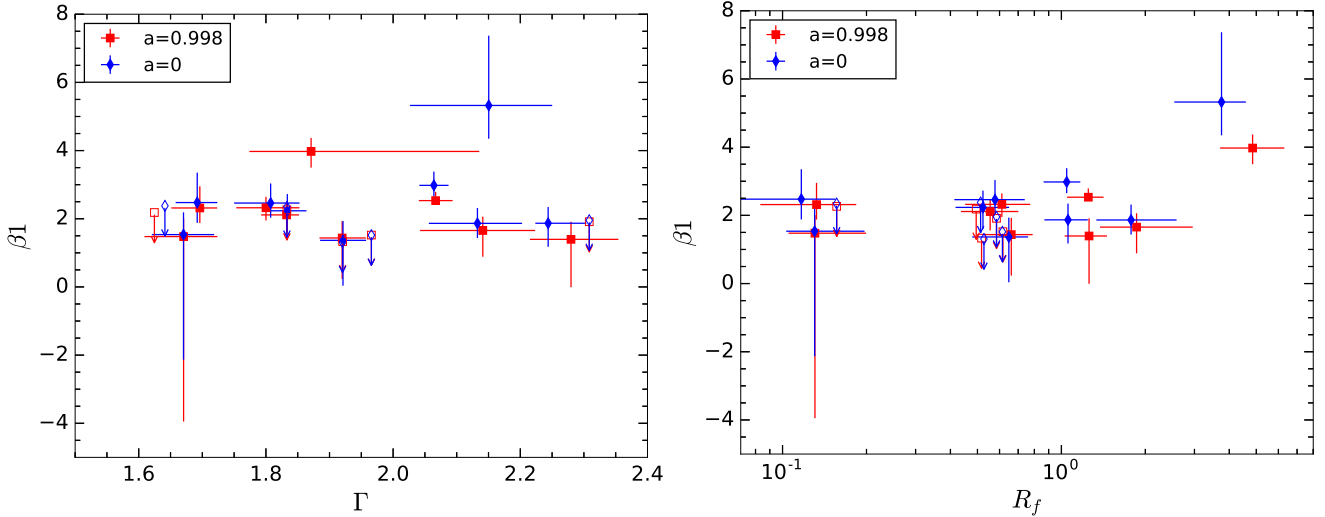


**Figure 5.** Plot showing emissivity index  $\beta_1$  vs.  $\Gamma$  (left) and  $\beta_1$  vs.  $R_f$  (right) for the sample. Filled red squares represent the values for  $a=0.998$ , and blue filled diamond-shaped data points represent the same for  $a=0$ . In case  $\beta_1$  is not constrained in the fit, the upper limit for the parameter values are denoted by open squares/diamonds with lower arrows.

mary emission) of about 1.7 and 0.5, respectively for mildly obscured ( $23 < \log N_{\mathrm{H}} < 24$ ) and lightly obscured ( $21 < \log N_{\mathrm{H}} < 22$ ) sources. For unabsorbed sources, they observed that the reflection strength is correlated to the photon index.

The correlation between relativistic reflection fraction and photon index is significant in our sample, and this can be explained as follows. The primary X-ray emission is produced by the inverse Compton scattering of the accretion disc photons by the hot electrons in the corona, and a portion of the same X-ray photons irradiates the disc producing the reflection features. Also, the slope of the power law is directly linked to the rate of cooling of the hot corona. Considering such a scenario, the more the input seed photons entering the corona, the stronger the cooling of plasma which results in a steeper X-ray power law. This results in a higher fraction of X-ray photons illuminating the accretion disc leading to larger reflection fraction. Since  $R_f$  represents

the intensity of the primary X-ray source irradiating the inner regions of the accretion disc relative to the intensity directly reaching the observer, the parameter, in turn, depends on the relative geometry of the accretion disc and the corona. Thus the observed  $R_f - \Gamma$  correlation could be a consequence of the change in the disc-corona geometry.

We also fitted the spectra of the sources IC 4329A and Swift J2127.4+5654 by varying the inner disc radius instead of fixing it at the innermost stable orbit. However,  $R_{\mathrm{in}}$  was not constrained, and we do not find any change in the reflection fraction.

Here, we are using the standard version of the RELXILL model that assumes the illumination profile of the accretion disc as a broken power law. In this model, the geometry of the illuminating source is not well defined. However, the emissivity index of the profile is expected to vary with different source heights and accretion disc radii. Hence we

can elucidate the geometry of the system from the emissivity index. Nevertheless, the emissivity index for the sample does not vary and is not constrained for a few sources. The plots for emissivity index versus  $\Gamma$  and  $R_f$  are shown in Fig. 5. However, the lamp post flavour of the model RELXILL-LLP has a well-specified geometry where an on-axis primary source is located above the black hole at a height  $h$ . We explored the possibility of constraining the geometry of the system using this model. We fitted the spectra of the sources IC 4329A and Swift J2127.4+5654 with RELXILL-LLP and obtained the source height in units of gravitational radius  $R_g$ . The height of the corona in Swift J2127.4+5654 is found to be  $\sim 39(50) R_g$  for  $a = 0(0.998)$  and in the case of IC 4329A the parameter is poorly constrained and has an upper limit of  $23(22) R_g$ . The inner disc radius  $R_{in}$  in both the sources are not constrained. We also note that neither the reflection fraction nor the photon index has changed significantly from the values we obtained for RELXILL model.

For assessing the exact geometry of the system, the current data and model seem to be inadequate. More appropriate modelling of AGN which can properly constrain the accretion disc and coronal geometry can reveal how the reflection fraction from the inner disc is determined by the geometry of the sources.

## 5 CONCLUSION

In this work, we analysed the reflection spectra of a sample of 14 Seyfert type 1 galaxies using the X-ray data from the *NuSTAR* observations. The X-ray spectra in the 3–79 keV band were modelled with RELXILL that explains the relativistic reflection features along with the primary X-ray emission, and the XILLVER component was used to model the features due to distant reflection. The relativistic reflection fraction  $R_f$  of the sample was obtained from the model RELXILL and is found to range from  $\sim 0.12(0.13)$  to  $\sim 3.75(4.85)$  for  $a = 0(0.998)$ . The parameters  $R_f$  and  $\Gamma$  show a significant positive correlation with a rank of  $0.83(0.65)$  (p-value  $\sim 0.0003(0.01)$ ). Since the slope of the X-ray power law is related to the rate of cooling of the plasma, steeper X-ray spectra indicate stronger cooling by the seed photons. The larger the area covered by the accretion disc as seen from the corona, the higher will be the seed photons entering the corona. This results in the steepening of the X-ray spectrum. Since the same accretion disc is responsible for the reflected emission, the larger area covered by the medium consequently enhances the reflection fraction. The observed  $R_f - \Gamma$  correlation is thus resulting from the change in disc-corona geometry of the AGN in our sample.

## 6 ACKNOWLEDGEMENT

We thank the anonymous referee for the useful comments and suggestions. This research has made use of data and/or software provided by the High Energy Astrophysics Science Archive Research Center (HEASARC), which is a service of the Astrophysics Science Division at NASA/GSFC and the High Energy Astrophysics Division of the Smithsonian Astrophysical Observatory. This work has made use of data obtained from the *NuSTAR* mission, a project led

by Caltech, funded by NASA and managed by NASA/JPL, and has utilised the NUSTARDAS software package, jointly developed by the ASDC, Italy and Caltech, USA. This research has made use of the NASA/IPAC Extragalactic Database (NED) which is operated by the Jet Propulsion Laboratory, California Institute of Technology, under contract with the National Aeronautics and Space Administration. We acknowledge the usage of the HyperLeda database (<http://leda.univ-lyon1.fr>). This research has made use of the SIMBAD database, operated at CDS, Strasbourg, France.

## References

- Ballantyne D. R., 2014, *MNRAS*, **437**, 2845
- Baloković M., et al., 2015, *ApJ*, **800**, 62
- Beloborodov A. M., 1999, *ApJ*, **510**, L123
- Boissay R., Ricci C., Paltani S., 2016, *A&A*, **588**, A70
- Brenneman L. W., et al., 2014, *ApJ*, **788**, 61
- Buisson D. J. K., et al., 2018, *MNRAS*, **480**, 3689
- Burton D., Ajello M., Greiner J., Comastri A., Merloni A., Gehrels N., 2011, *ApJ*, **728**, 58
- Dadina M., 2008, *A&A*, **485**, 417
- Dauser T., Wilms J., Reynolds C. S., Brenneman L. W., 2010, *MNRAS*, **409**, 1534
- Dauser T., et al., 2012, *MNRAS*, **422**, 1914
- Dauser T., García J., Parker M. L., Fabian A. C., Wilms J., 2014, *MNRAS*, **444**, L100
- Dauser T., García J., Walton D. J., Eikmann W., Kallman T., McClintock J., Wilms J., 2016, *A&A*, **590**, A76
- Del Moro A., et al., 2017, *ApJ*, **849**, 57
- Dovčiak M., Karas V., Yaqoob T., 2004, *ApJS*, **153**, 205
- Fabian A. C., Ross R. R., 2010, *Space Sci. Rev.*, **157**, 167
- Fabian A. C., Vaughan S., 2003, *MNRAS*, **340**, L28
- Fabian A. C., Rees M. J., Stella L., White N. E., 1989, *MNRAS*, **238**, 729
- Fabian A. C., Iwasawa K., Reynolds C. S., Young A. J., 2000, *PASP*, **112**, 1145
- Fabian A. C., et al., 2002, *MNRAS*, **335**, L1
- Fabian A. C., Lohfink A., Kara E., Parker M. L., Vasudevan R., Reynolds C. S., 2015, *MNRAS*, **451**, 4375
- Fabian A. C., Lohfink A., Belmont R., Malzac J., Coppi P., 2017, *MNRAS*, **467**, 2566
- Frederick S., Kara E., Reynolds C., Pinto C., Fabian A., 2018, *ApJ*, **867**, 67
- Gallo L. C., et al., 2019, *MNRAS*, **484**, 4287
- García J., Kallman T. R., 2010, *ApJ*, **718**, 695
- García J., Kallman T. R., Mushotzky R. F., 2011, *ApJ*, **731**, 131
- García J., et al., 2014, *ApJ*, **782**, 76
- George I. M., Fabian A. C., 1991, *MNRAS*, **249**, 352
- Ghosh R., Dewangan G. C., Mallick L., Raychaudhuri B., 2018, *MNRAS*, **479**, 2464
- Gliozzi M., Sambruna R. M., Eracleous M., Yaqoob T., 2007, *The Astrophysical Journal*, **664**, 88
- Gofford J., Reeves J. N., Tombesi F., Braito V., Turner T. J., Miller L., Cappi M., 2013, *MNRAS*, **430**, 60
- Haardt F., Maraschi L., 1993, *ApJ*, **413**, 507
- Harrison F. A., et al., 2013, *ApJ*, **770**, 103
- Kalberla P. M. W., Burton W. B., Hartmann D., Arnal E. M., Bajaja E., Morras R., Pöppel W. G. L., 2005, *A&A*, **440**, 775
- Kallman T., Bautista M., 2001, *ApJS*, **133**, 221
- Landt H., et al., 2017, *MNRAS*, **464**, 2565
- Lee J. C., Iwasawa K., Houck J. C., Fabian A. C., Marshall H. L., Canizares C. R., 2002, *ApJ*, **570**, L47
- Lightman A. P., White T. R., 1988, *ApJ*, **335**, 57

- Longinotti A. L., Bianchi S., Santos-Lleo M., Rodríguez-Pascual P., Guainazzi M., Cardaci M., Pollock A. M. T., 2007, *A&A*, **470**, 73
- Longinotti A. L., et al., 2019, *ApJ*, **875**, 150
- Lubiński P., et al., 2016, *MNRAS*, **458**, 2454
- Makarov D., Prugniel P., Terekhova N., Courtois H., Vauglin I., 2014, *A&A*, **570**, A13
- Malzac J., Beloborodov A. M., Poutanen J., 2001, *MNRAS*, **326**, 417
- Marinucci A., et al., 2014, *MNRAS*, **440**, 2347
- Marinucci A., et al., 2015, *MNRAS*, **447**, 160
- Marinucci A., Tortosa A., NuSTAR AGN Physics Working Group 2016, *Astronomische Nachrichten*, **337**, 490
- Markowitz A., Reeves J. N., Braito V., 2006, *ApJ*, **646**, 783
- Matt G., Perola G. C., Piro L., 1991, *A&A*, **247**, 25
- Matt G., et al., 2015, *MNRAS*, **447**, 3029
- Mattson B. J., Weaver K. A., Reynolds C. S., 2007, *ApJ*, **664**, 101
- McKernan B., Yaqoob T., 2004, *ApJ*, **608**, 157
- Middei R., Vagnetti F., Tombesi F., Bianchi S., Marinucci A., Ursini F., Tortosa A., 2018, *A&A*, **618**, A167
- Miller L., Turner T. J., Reeves J. N., 2008, *A&A*, **483**, 437
- Miniutti G., et al., 2007, *PASJ*, **59**, 315
- Mizumoto M., Ebisawa K., Tsujimoto M., Done C., Hagino K., Odaka H., 2019, *MNRAS*, **482**, 5316
- Molina M., et al., 2009, *MNRAS*, **399**, 1293
- Nandra K., Pounds K. A., 1994, *MNRAS*, **268**, 405
- Nandra K., Pounds K. A., Stewart G. C., 1990, *MNRAS*, **242**, 660
- Nandra K., George I. M., Mushotzky R. F., Turner T. J., Yaqoob T., 1997, *ApJ*, **477**, 602
- Nandra K., O'Neill P. M., George I. M., Reeves J. N., 2007, *MNRAS*, **382**, 194
- Nardini E., Fabian A. C., Reis R. C., Walton D. J., 2011, *MNRAS*, **410**, 1251
- Nardini E., Porquet D., Reeves J. N., Braito V., Lobban A., Matt G., 2016, *ApJ*, **832**, 45
- Page K. L., Reeves J. N., O'Brien P. T., Turner M. J. L., 2005, *MNRAS*, **364**, 195
- Pahari M., McHardy I. M., Mallick L., Dewangan G. C., Misra R., 2017, *MNRAS*, **470**, 3239
- Panagiotou C., Walter R., 2019, *Astronomy and Astrophysics*, **626**, A40
- Papadakis I. E., Brinkmann W., Page M. J., McHardy I., Uttley P., 2007, *A&A*, **461**, 931
- Parker M. L., et al., 2014, *MNRAS*, **443**, 1723
- Patrick A. R., Reeves J. N., Porquet D., Markowitz A. G., Lobban A. P., Terashima Y., 2011, *MNRAS*, **411**, 2353
- Porquet D., et al., 2018, *A&A*, **609**, A42
- Press W. H., Teukolsky S. A., Vetterling W. T., Flannery B. P., 1992, Numerical recipes in FORTRAN. The art of scientific computing
- Rani P., Stalin C. S., 2018, *Journal of Astrophysics and Astronomy*, **39**, 15
- Reeves J. N., Turner M. J. L., 2000, *MNRAS*, **316**, 234
- Reynolds C. S., 1999, in Poutanen J., Svensson R., eds, Astronomical Society of the Pacific Conference Series Vol. 161, High Energy Processes in Accreting Black Holes. p. 178 ([arXiv:astro-ph/9810018](https://arxiv.org/abs/astro-ph/9810018))
- Reynolds C. S., Nowak M. A., 2003, *Phys. Rep.*, **377**, 389
- Reynolds C. S., Fabian A. C., Inoue H., 1995, *MNRAS*, **276**, 1311
- Reynolds C. S., Brenneman L. W., Lohfink A. M., Trippe M. L., Miller J. M., Fabian A. C., Nowak M. A., 2012, *ApJ*, **755**, 88
- Ricci C., Walter R., Courvoisier T. J. L., Paltani S., 2011, *A&A*, **532**, A102
- Shemmer O., Brandt W. N., Netzer H., Maiolino R., Kaspi S., 2008, *ApJ*, **682**, 81
- Steiner J. F., et al., 2011, *MNRAS*, **416**, 941
- Tanaka Y., et al., 1995, *Nature*, **375**, 659
- Tombesi F., Cappi M., Reeves J. N., Palumbo G. G. C., Yaqoob T., Braito V., Dadina M., 2010, *A&A*, **521**, A57
- Tombesi F., Cappi M., Reeves J. N., Palumbo G. G. C., Braito V., Dadina M., 2011, *ApJ*, **742**, 44
- Tortosa A., et al., 2017, *MNRAS*, **466**, 4193
- Tortosa A., Bianchi S., Marinucci A., Matt G., Petrucci P. O., 2018, *A&A*, **614**, A37
- Ueda Y., Ebisawa K., Done C., 1994, *PASJ*, **46**, 107
- Wenger M., et al., 2000, *A&AS*, **143**, 9
- Wilkins D. R., Gallo L. C., 2015, *MNRAS*, **448**, 703
- Wilms J., Reynolds C. S., Begelman M. C., Reeves J., Molendi S., Staubert R., Kendziorra E., 2001, *MNRAS*, **328**, L27
- Xu Y., Baloković M., Walton D. J., Harrison F. A., García J. A., Koss M. J., 2017, *ApJ*, **837**, 21
- Yaqoob T., Padmanabhan U., 2004, *ApJ*, **604**, 63
- Zappacosta L., et al., 2018, *ApJ*, **854**, 33
- Zdziarski A. A., Lubiński P., Smith D. A., 1999, *MNRAS*, **303**, L11
- Zoghbi A., et al., 2015, *ApJ*, **799**, L24

## APPENDIX A: RESIDUAL PLOTS

The residuals for the spectral fits using the model CONSTANT  $\times$  TBABS  $\times$  POWERLAW is shown in Fig. A1.

## APPENDIX B: SPECTRAL FITTING PLOTS

The broadband spectral fits and residuals using the final best-fit model (for  $a = 0$ ) for the whole sample is plotted in Fig. B1.

This paper has been typeset from a *TeX/LaTeX* file prepared by the author.

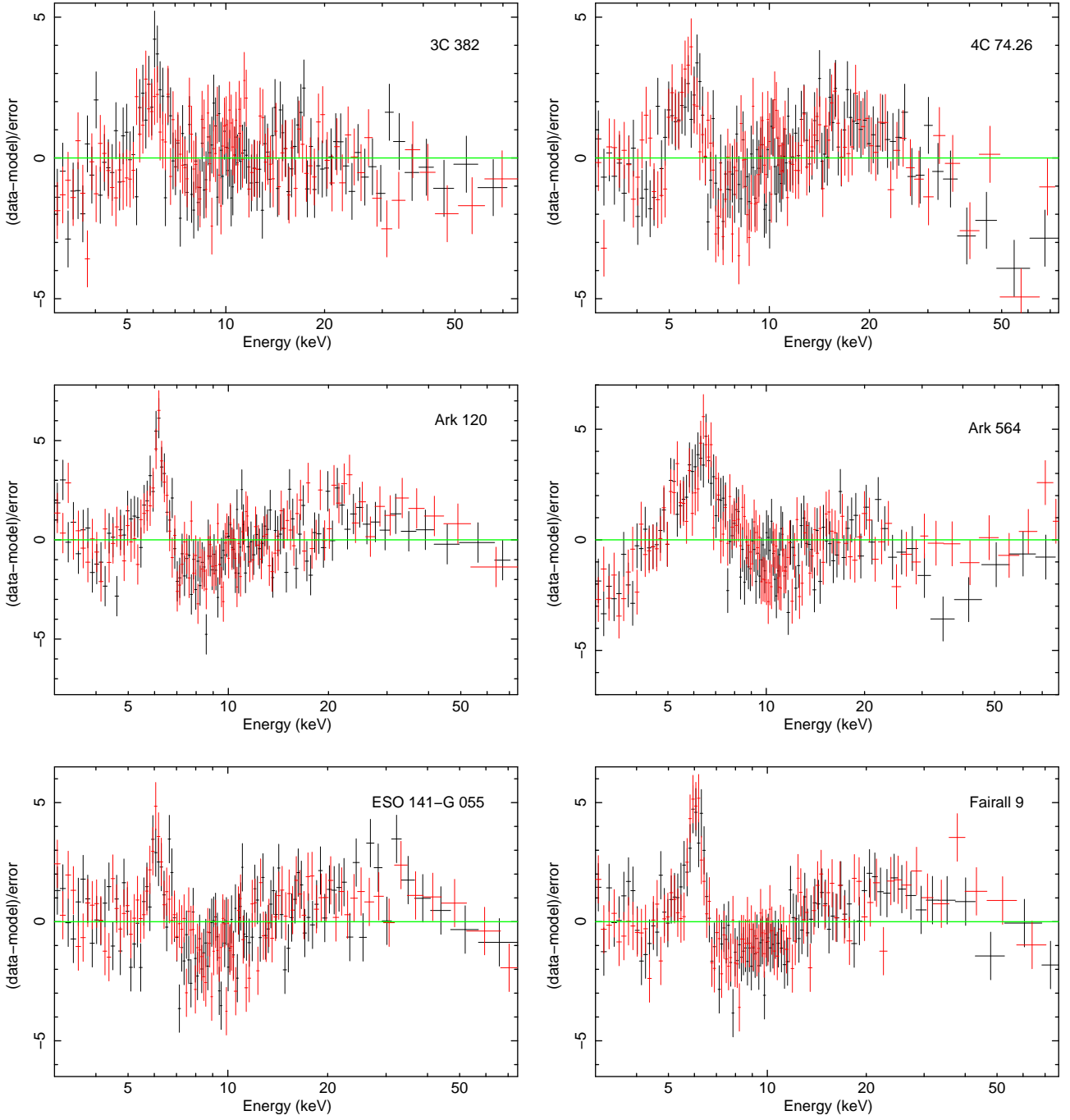


**Figure A1.** Plots showing the residuals for the model `CONSTANT`×`TBABS`×`POWERLAW` fitted over the 3–79 keV range. All the data have been rebinned for plotting purpose.

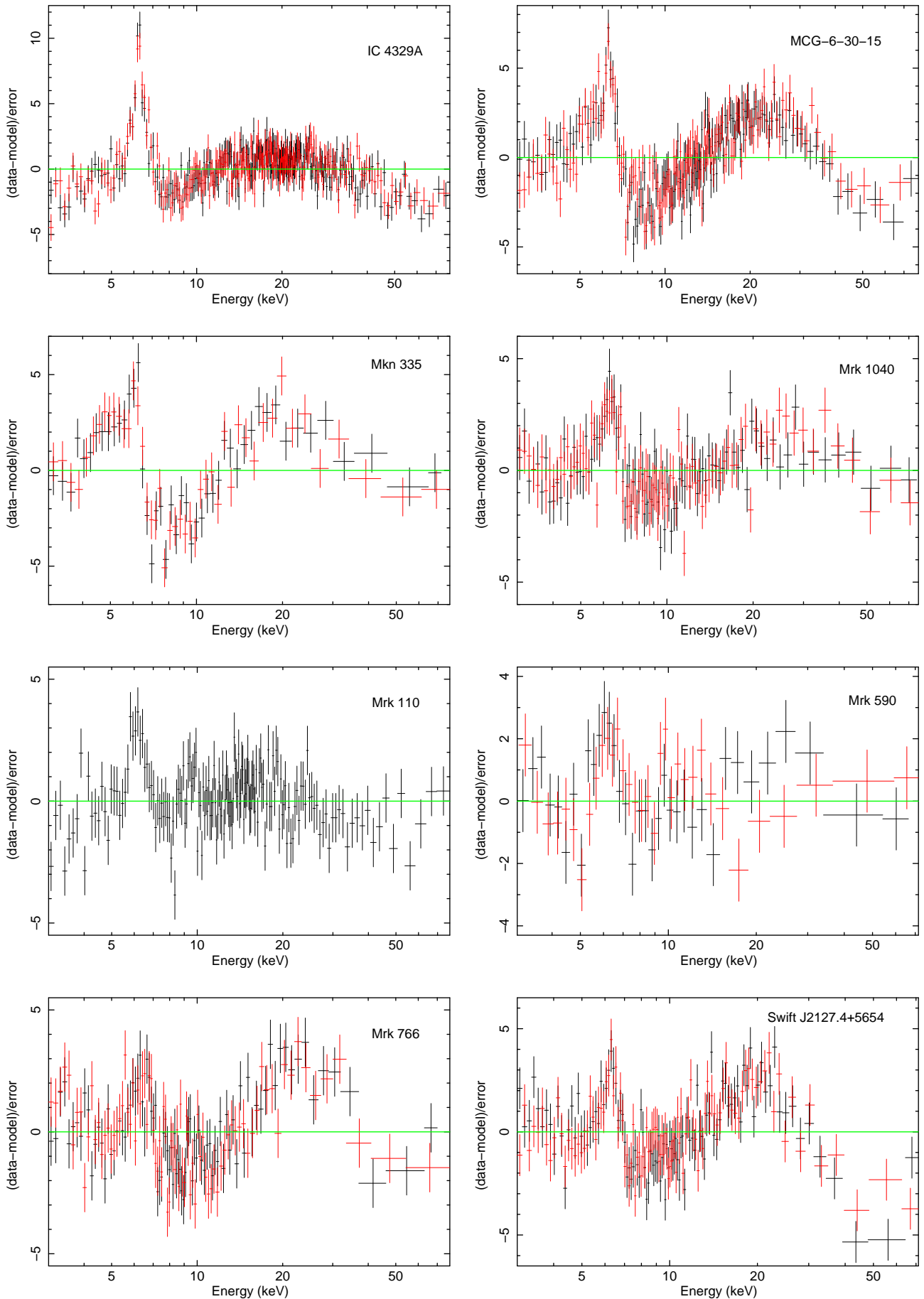
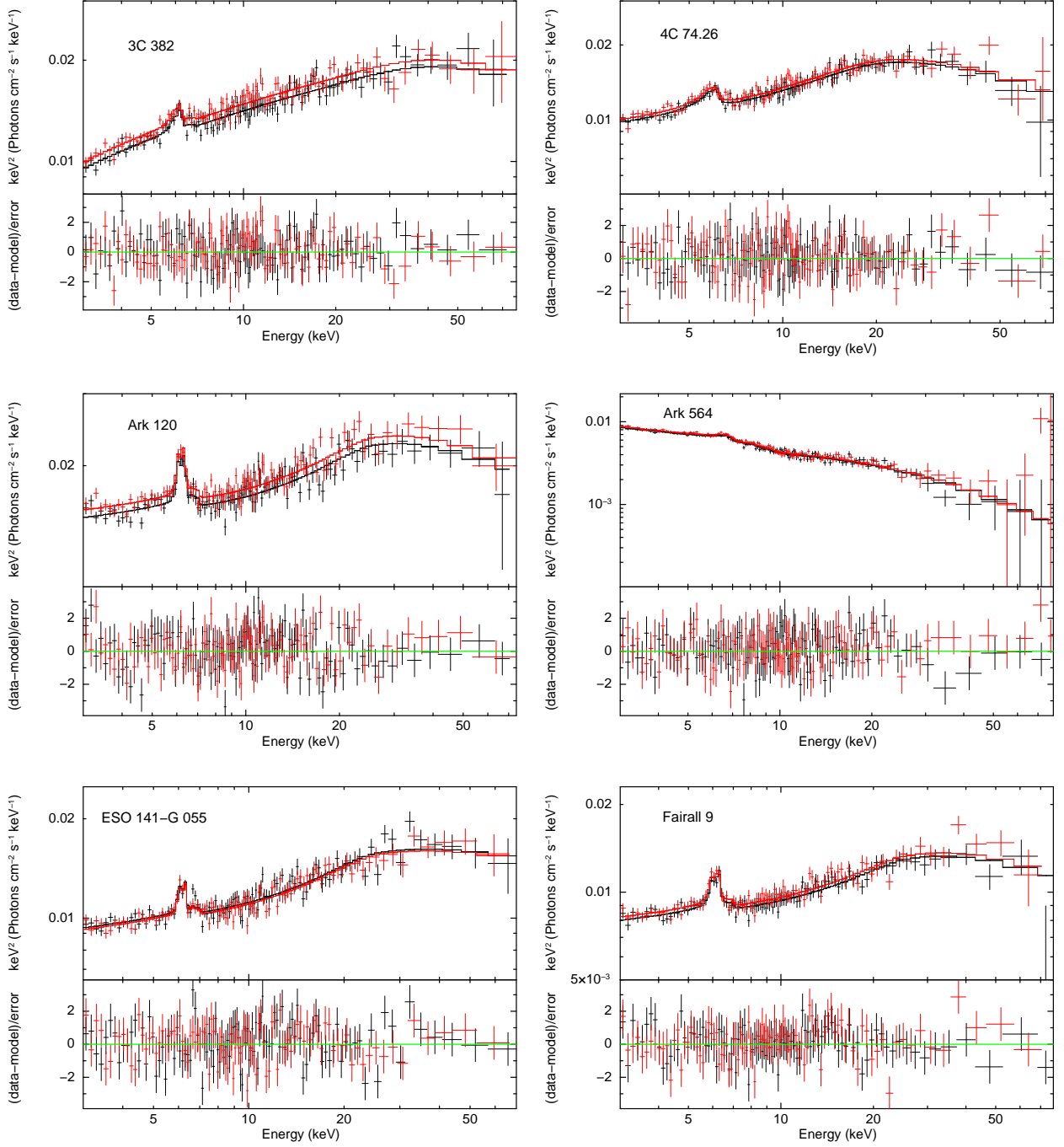


Figure A1 (continued)



**Figure B1.** Spectral fitting plots for the sample. Upper panels: The unfolded spectra and the best-fit models (CONSTANT  $\times$  TBABS  $\times$  RELXILL or CONSTANT  $\times$  TBABS( RELXILL + XILLVER)). Lower panels: The residuals of the spectral fit.

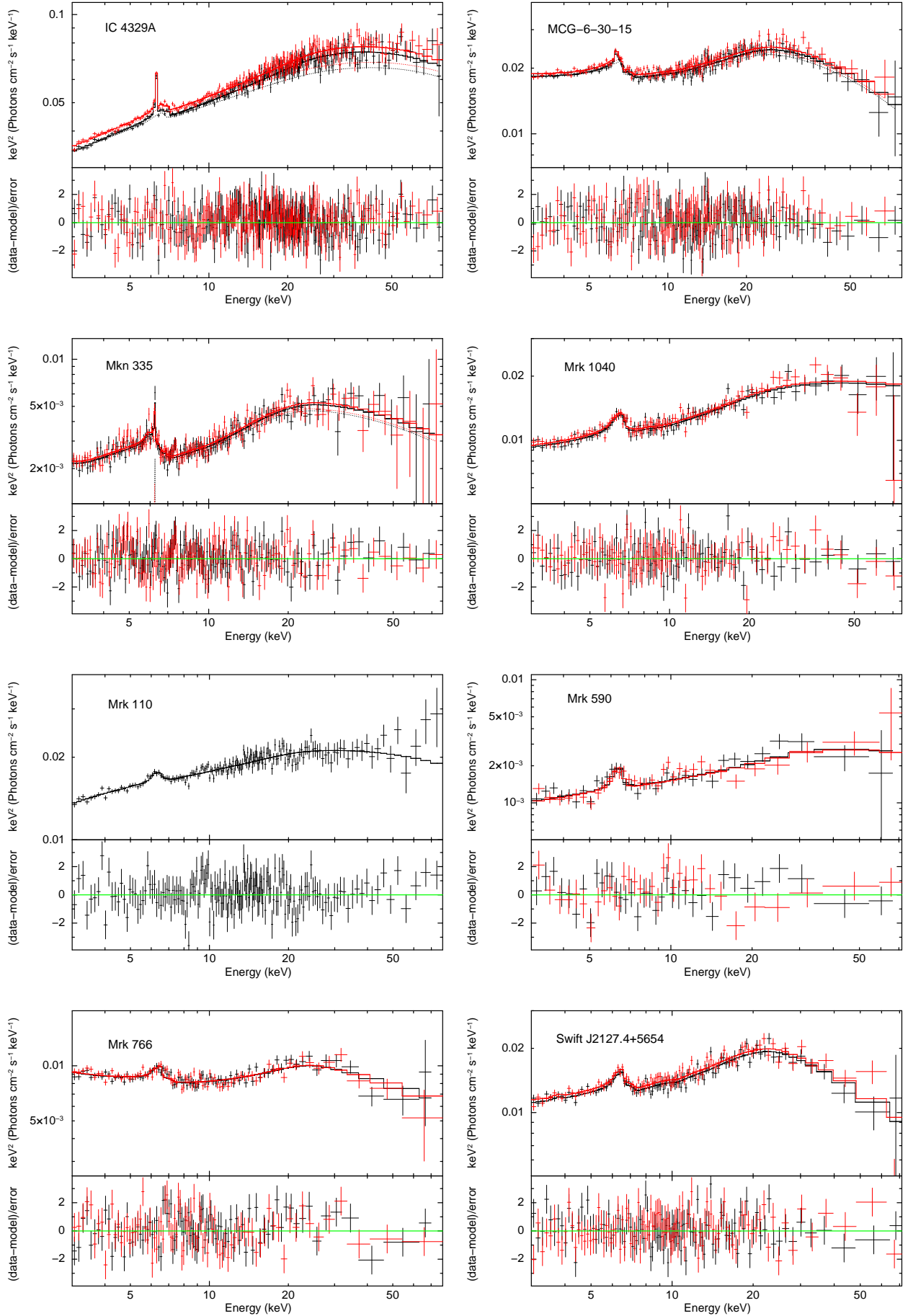


Figure B1 (continued)